

# DISCRETE DISTRIBUTION NETWORKS

**Anonymous authors**

Paper under double-blind review

## ABSTRACT

We introduce a novel generative model, the Discrete Distribution Networks (DDN), that approximates data distribution using hierarchical discrete distributions. We posit that since the features within a network inherently capture distributional information, enabling the network to generate multiple samples simultaneously, rather than a single output, may offer an effective way to represent distributions. Therefore, DDN fits the target distribution, including continuous ones, by generating multiple discrete sample points. To capture finer details of the target data, DDN selects the output that is closest to the Ground Truth (GT) from the coarse results generated in the first layer. This selected output is then fed back into the network as a condition for the second layer, thereby generating new outputs more similar to the GT. As the number of DDN layers increases, the representational space of the outputs expands exponentially, and the generated samples become increasingly similar to the GT. This hierarchical output pattern of discrete distributions endows DDN with unique property: more general zero-shot conditional generation. We demonstrate the efficacy of DDN and its intriguing properties through experiments on CIFAR-10 and FFHQ.

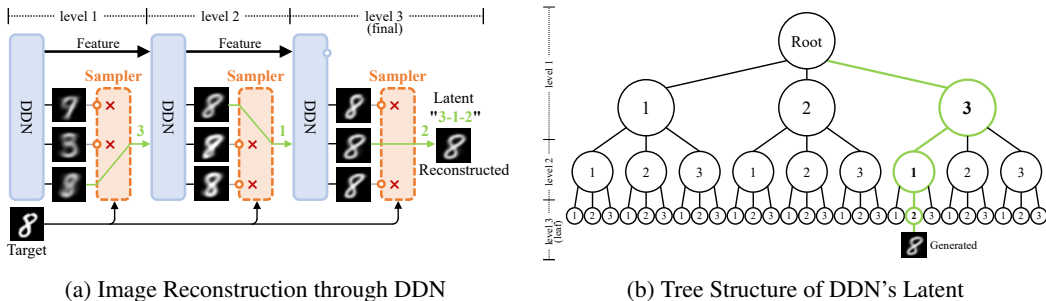


Figure 1: (a) Illustrates the process of image reconstruction and latent acquisition in DDN. Each layer of DDN outputs  $K$  distinct images to approximate the distribution  $P(X)$ . The sampler then selects the image most similar to the target from these and feeds it into the next DDN layer. As the number of layers increases, the generated images become increasingly similar to the target. For generation tasks, the sampler is simply replaced with a random choice operation. (b) Depicts the tree-structured representation space of DDN’s latent variables. Each sample can be mapped to a leaf node on this tree.

## 1 INTRODUCTION

With the advent of ChatGPT Brown et al. (2020) and DDPM Ho et al. (2020), deep generative models have become increasingly popular and significant in everyday life. However, modeling the complex and diverse high-dimensional data distributions is challenging. Previous methods Kingma & Welling (2014); Radford et al. (2016); Kingma & Dhariwal (2018); Goyal et al. (2021); Song et al. (2021); Shocher et al. (2024); Graves et al. (2023) have each demonstrated their unique strengths and characteristics in modeling these distributions. In this work, we propose a novel approach to model the target distribution, where the core idea is to generate multiple samples simultaneously, allowing the network to directly output an approximate discrete distribution. Hence, we name our method

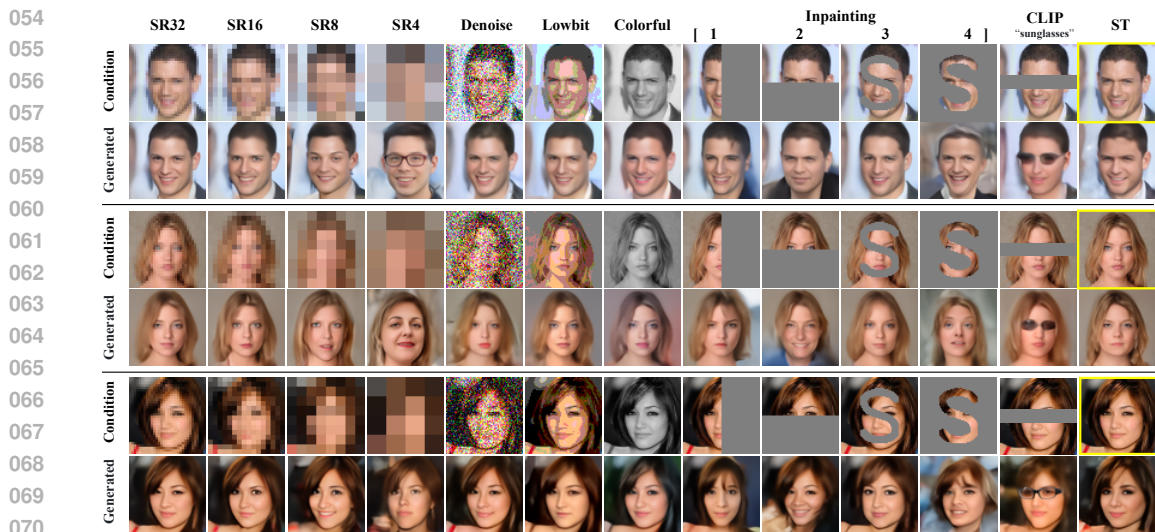


Figure 2: **DDN enables more general zero-shot conditional generation.** DDN supports zero-shot conditional generation across non-pixel domains, and notably, without relying on gradient, such as text-to-image generation using a black-box CLIP model Radford et al. (2021). Images enclosed in yellow borders serve as the ground truth. The abbreviations in the table header correspond to their respective tasks as follows: ‘SR’ stands for Super-Resolution, with the following digit indicating the resolution of the condition. ‘ST’ denotes Style Transfer, which computes Perceptual Losses with the condition according to Johnson et al. (2016).

Discrete Distribution Networks (DDN). DDN embraces a core concept as simple as autoregressive models, offering another straightforward and effective form for generative models.

Most generative models applied in real-world scenarios are conditional generative models. Taking image generation as an example, these models generate corresponding images based on content provided by users, such as images to be edited, reference images Saharia et al. (2021), text descriptions, hand-drawn editing strokes Voynov et al. (2022), sketches, and so on. Current mainstream generative models Rombach et al. (2021); Ramesh et al. (2022); Zhang et al. (2023) typically require training separate models and parameters for each condition. These models are restricted to fixed condition formats and lack the flexibility to adjust the influence of each condition dynamically, thereby limiting users’ creative freedom.

Recent works have attempted to address this issue through zero-shot conditional generation (ZSCG). However, these methods either only support conditions in the same pixel domain as the training data Wang et al. (2022); Lugmayr et al. (2022); Meng et al. (2021); Nair et al. (2023) or depend on discriminative models to supply gradients during generation Yu et al. (2023). In contrast, DDN supports a wide range of ZSCG tasks, encompassing both pixel-domain and non-pixel-domain conditions, as shown in fig. 2. To the best of our knowledge, DDN is the first generative model capable of performing zero-shot conditional generation in non-pixel domains without relying on gradient information. This implies that DDN can achieve ZSCG solely based on black-box discriminative models.

The core concept of Discrete Distribution Networks (DDN) is to approximate the distribution of training data using a multitude of discrete sample points. The secret to generating diverse samples lies in the network’s ability to concurrently generate multiple samples ( $K$ ). This is perceived as the network outputting a discrete distribution. All generated samples serve as the sample space for this discrete distribution. Typically, each sample in this discrete distribution has an equal probability mass of  $1/K$ . Our goal is to make this discrete distribution as close as possible to the target dataset.

To accurately fit the target distribution of large datasets, a substantial representational space is required. In the most extreme scenario, this space must be larger than the number of training data samples. However, current neural networks lack the feasibility to generate such a vast number of samples simultaneously. Therefore, we adopt a strategy from autoregressive models Van Den Oord et al. (2016) and partition this large space into a hierarchical conditional probability model. Each layer of this model needs only a small number of outputs. We then select one of these outputs as the

output for that layer and use it as conditional input to the next layer. As a result, the output of the next layer will be more closely related to the selected conditional sample. If the number of layers is  $L$  and the number of outputs per layer is  $K$ , then the output space of the network is  $K^L$ . Due to its exponential nature, this output space will be much larger than the number of samples in the dataset. fig. 1 shows how DDN generates images.

We posit that the contributions of this paper are as follows: (1) We introduce a novel generative model, termed Discrete Distribution Networks (DDN), which exhibit a more straightforward and streamlined principle and form. (2) For training the DDN, we propose the “Split-and-Prune” optimization algorithm, and a range of practical techniques. (3) We conduct preliminary experiments and analysis on the DDN, showcasing its intriguing properties and capabilities, such as zero-shot conditional generation and highly compact representations.

## 2 RELATED WORK

**Deep Generative Model.** Generative Adversarial Networks (GANs) Radford et al. (2016); Brock et al. (2019) and Variational Autoencoders (VAEs) Kingma & Welling (2014); van den Oord et al. (2018) are two early successful generative models. GANs reduce the divergence between the generated sample distribution and the target distribution through a game between the generator and discriminator. However, regular GANs cannot map samples back to the latent space, thus they cannot reconstruct samples. VAEs encode data into a simple distribution’s latent space through an Encoder, and the Decoder is trained to reconstruct the original data from this simple distribution’s latent space. Autoregressive models van den Oord et al. (2016), with their simple principles and methods, model the target distribution by decomposing the target data into conditional probability distributions of each component. They can also compute the exact likelihood of target samples. However, the efficiency of these models is reduced when dealing with image data, which is not suitable to be decomposed into a sequence of components. Normalizing flow Kingma & Dhariwal (2018) is another class of generative models that can compute the likelihood. They use invertible networks to construct a mapping from samples to a noise space, and during the generation stage, they map back from noise to samples. Energy Based Models (EBM) Goyal et al. (2021); Song et al. (2021) with their high-quality and rich generative results, have led to the rise of diffusion models. However, their multi-step iterative generation process requires substantial computational resources. The recent Idempotent Generative Network Shocher et al. (2024) introduces a novel approach by training a neural network to be idempotent, mapping any input to the target distribution effectively.

**Connections to VQ-VAE.** While both VQ-VAE van den Oord et al. (2018) and DDN involve discrete representations, they differ significantly in their approach and capabilities. VQ-VAE enhances the traditional VAE by replacing the continuous latent space with discrete codebooks, thus achieving a more compact representation. VQ-VAE-2 Razavi et al. (2019) further improves this by employing a multi-scale hierarchical structure, thereby enhancing its representational power. However, the discrete representation in VQ-VAE remains two-dimensional, potentially leading to redundant information. Furthermore, VQ-VAE and its successors still rely on an additional prior network for generative modeling in the latent space. Notably, DDN can also serve as this prior model to effectively model the latent space of VQ-VAE. Other distinctions between DDN and VQ-VAE include the absence of an encoder and codebook in DDN, as well as its capacity for Zero-Shot Conditional Generation. VQ-VAEs are known to encounter codebook collapse, a problem that some researchers have addressed by reinitializing unused codes near frequently used ones Williams et al. (2020); Dhariwal et al. (2020). Our Split-and-Prune algorithm shares a similar core idea, albeit with some differences. While the reinitialization method aims to balance code usage to mitigate codebook collapse, our goal is to align the discrete distribution output by our network as closely as possible to the target distribution.

## 3 DISCRETE DISTRIBUTION NETWORKS

**Network architecture.** Figure 3a illustrates the overall structure of the DDN, comprised of Neural Network Blocks and Discrete Distribution Layers (DDL). Each DDL contains  $K$  output nodes, each of which is a set of  $1 \times 1$  convolutions responsible for transforming the feature into the corresponding

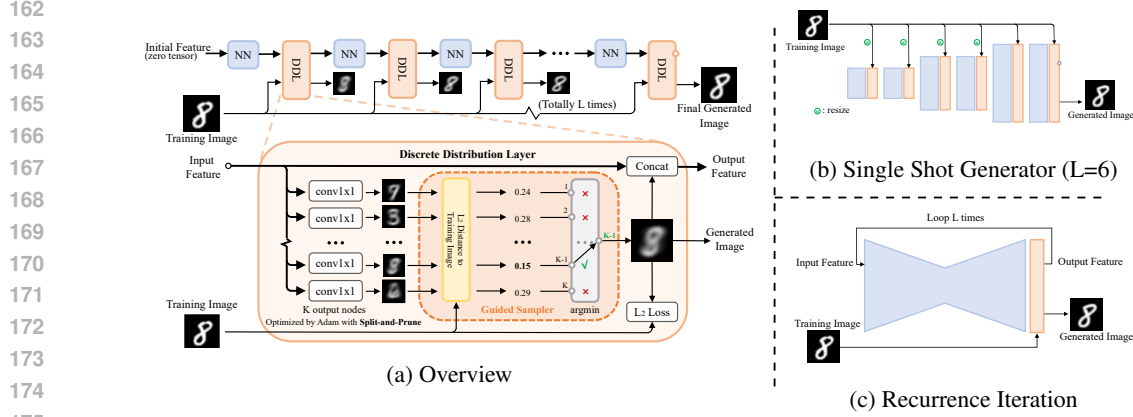


Figure 3: **Schematic of Discrete Distribution Networks (DDN).** (a) The data flow during the training phase of DDN is shown at the top. As the network depth increases, the generated images become increasingly similar to the training images. Within each Discrete Distribution Layer (DDL),  $K$  samples are generated, and the one closest to the training sample is selected as the generated image for loss computation. These  $K$  output nodes are optimized using Adam with Split-and-Prune method. The right two figures shown the two model paradigms supported by DDN. (b) Single Shot Generator Paradigm: Each neural network layer and DDL has independent weights. (c) Recurrence Iteration Paradigm: All neural network layers and DDLs share weights. For inference, replacing the Guided Sampler in the DDL with a random choice enables the generation of new images.

output image. The parameters of these  $1 \times 1$  convolutions are optimized by Adam with Split-and-Prune. The  $K$  images generated by the  $K$  output nodes are inputted into the Guided Sampler. The Guided Sampler selects the image with the smallest L2 distance to the training image, which serves as the output of the current layer and is used to calculate the L2 loss with the training image. Simultaneously, the selected image is concatenated back into the feature, acting as the condition for the next block. The index (depicted in green as “ $K-1$ ” in fig. 3a) of the selected image represents the latent value of the training sample at this layer. Through the guidance of the Guided Sampler layer by layer, the image generated by the network progressively becomes more similar to the training sample until the final layer produces an approximation of the training sample.

For computational efficiency, we adopted a decoder structure similar to the generator in GANs for coarse-to-fine image generation, as shown in fig. 3b. We refer to this as the Single Shot Generator **which is our default choice**. As each layer of DDN can naturally input and output RGB domain data, DDN seamlessly support the Recurrence Iteration Paradigm fig. 3c.

**Objective function.** The DDN model consists of  $L$  layers of Discrete Distribution Layers (DDL). For a given layer  $l$ , denoted as  $f_l$ , the input is the selected sample from the previous layer,  $\mathbf{x}_{l-1}^*$ . The layer generates  $K$  new samples,  $f_l(\mathbf{x}_{l-1}^*)$ , from which we select the sample  $\mathbf{x}_l^*$  that is closest to the current training sample  $\mathbf{x}$ , along with its corresponding index  $k_l^*$ . The loss  $J_l$  for this layer is then computed only on the selected sample  $\mathbf{x}_l^*$ .

$$k_l^* = \operatorname{argmin}_{k \in \{1, \dots, K\}} \|f_l(\mathbf{x}_{l-1}^*)[k] - \mathbf{x}\|^2 \quad (1)$$

$$\mathbf{x}_l^* = f_l(\mathbf{x}_{l-1}^*)[k_l^*] \quad ; \quad J_l = \|\mathbf{x}_l^* - \mathbf{x}\|^2 \quad (2)$$

Here,  $\mathbf{x}_0^* = \mathbf{0}$  represents the initial input to the first layer. For simplicity, we omit the details of input/output feature, neural network blocks and transformation operations in the equations.

By recursively unfolding the above equations, we can derive the latent variable  $\mathbf{k}_{1:L}^*$  and the global objective function  $J$ .

$$\mathbf{k}_{1:L}^* = [k_1^*, k_2^*, \dots, k_L^*] = \left[ \operatorname{argmin}_{k \in \{1, \dots, K\}} \|\mathcal{F}([\mathbf{k}_{1:l-1}^*, k]) - \mathbf{x}\|^2 \right]_{l=1}^L \quad (3)$$

216  
217  
218  
219  
220  
221  
222  
223  
224  
225  
226  
227  
228  
229  
230  
231  
232  
233  
234  
235  
236  
237

$$J = \frac{1}{L} \sum_{l=1}^L \|\mathcal{F}(\mathbf{k}_{1:l}^*) - \mathbf{x}\|^2 \tag{4}$$

Here,  $\mathcal{F}$  represents the composite function formed from  $f_l$ , defined as:  $\mathcal{F}(\mathbf{k}_{1:l}) = f_l(f_{l-1}(\dots f_1(\mathbf{x}_0)[k_1] \dots)[k_{l-1}])[k_l]$ . Finally, we average the L2 loss across all layers to obtain the final loss for the entire network.

**How to generation.** When the network performs the generation task, replacing the Guided Sampler with a random choice enables image generation. Given the exponential representational space of  $K^L$  sample space and the limited number of samples in the training set, the probability of sampling an image with the same latent space as those in the training set is also exponentially low. For image reconstruction tasks, the process is almost identical to the training process, only substituting the training image with the target image to be reconstructed and omitting the L2 Loss part from the training process. The Final Generated Image in fig. 3a represents the final reconstruction result. The indices of the selected samples along the way form the latent representation of the target image  $\mathbf{k}_{1:L}^*$ , same as eq. (3). Therefore, the latent  $\mathbf{k}_{1:L}^*$  is a sequence of integers with length  $L$ , which we regard as the hierarchical discrete representation of the target sample. The latent space exhibits a tree structure with  $L$  layers and  $K$  degrees per node, where each leaf node represents a sample space, and its latent representation indicates the indices of all nodes along the path to this leaf node, as shown in fig. 1b. In the latent sequence, values placed earlier correspond to higher-level nodes in the tree, controlling the low-frequency information of the output sample, while later values tend to affect high-frequency information.

238  
239  
240  
241  
242  
243  
244  
245  
246

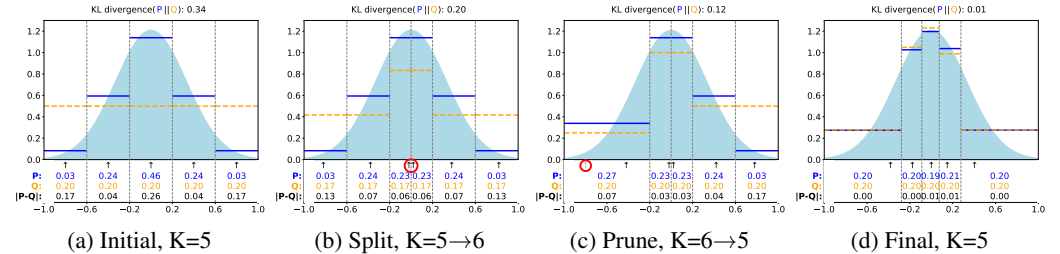


Figure 4: **Illustration of the principle behind the Split-and-Prune operation.** For example in (a), the light blue bell-shaped curve represents a one-dimensional target distribution. The 5 “↑” under the x-axis are the initial values from a uniform distribution of 5 output nodes, which divide the entire space into 5 parts using midpoints between adjacent nodes as boundaries (i.e., vertical gray dashed lines). Each part corresponds to the range represented by this output node on the continuous space  $x$ . Below each node are three values:  $P$  stands for the relative frequency of the ground truth falling within this node’s range during training;  $Q$  refers to the probability mass of this sample (node) in the discrete distribution output by the model during the generation phase, which is generally equal for each sample, i.e.,  $1/K$ . The bottom-most value denotes the difference between  $P$  and  $Q$ . Colorful horizontal line segments represent the average probability density of  $P$ ,  $Q$  within corresponding intervals. In (b), the Split operation selects the node with the highest  $P$  (circled in red). In (c), the Prune operation selects the node with the smallest  $P$  (circled in red). In (d), through the combined effects of loss and Split-and-Prune operations, the distribution of output nodes moves towards final optimization. From the observed results, the KL divergence ( $KL(P||Q)$ ) consistently decreases as the operation progresses, and the yellow line increasingly approximates the light blue target distribution.

262

### 3.1 OPTIMIZATION WITH SPLIT-AND-PRUNE

263  
264  
265  
266  
267  
268  
269

We have observed two primary issues resulting from each layer calculating loss only with the closest output samples to the ground truth (GT). Firstly, a problem similar to the “dead codebooks” in VQ-VAE arises, wherein output nodes that are not selected for a long time receive no gradient updates. During generation, these “dead nodes” are selected with equal probability, leading to poor output. The second issue is the probability density shift. For instance, in a one-dimensional asymmetric bimodal distribution, the target distribution is a mixture of two thin and tall Gaussian distribution

functions, with one larger and one smaller peak. The means of these two peaks are -1 and 1, respectively. Therefore, half of the output samples with initial values less than 0 will be matched with samples from the larger peak and optimized towards the larger Gaussian distribution. Meanwhile, the other half of the output samples with values greater than 0 will be optimized towards the smaller Gaussian. A problem arises as the large and small peaks carry different probability masses but occupy equal portions of the output samples, resulting in the same sampling probability during generation.

Inspired by the theory of evolution and genetic algorithms Katoch et al. (2021), we propose the Split-and-Prune algorithm to address the above issues, as outlined in algorithm 1. The Split operation targets nodes frequently matched by training samples, while the Prune operation addresses the issue of “dead nodes”, similar to those in Williams et al. (2020); Dhariwal et al. (2020). These nodes are akin to species in evolution, subject to diversification and extinction. During training, we track the frequency with which each node is matched by training samples. For nodes with excessive frequency, we execute the Split operation, cloning the node into two new nodes, each inheriting half of the old node’s frequency. Although these two new nodes have identical parameters and outputs, the next matched training sample will only be associated with one node. Therefore, the loss and gradient only affect one node’s parameters. Consequently, their parameters and outputs exhibit slight differences, dividing the old node’s match space into two. In subsequent training, the outputs of the two new nodes will move towards the centers of their respective spaces under the influence of the loss, diverging to produce more diverse outputs. For nodes with low matching frequency (dead nodes), we implement the Prune operation, removing them outright. fig. 4 illustrates the process of the Split-and-Prune operation and how it reduces the distance between the discrete distribution represented by the Output Nodes and the target distribution. The efficacy of the Split-and-Prune optimization algorithm is validated through examples of fitting 2d density maps in fig. 17.

### 3.2 APPLICATIONS

**Zero-Shot Conditional Generation (ZSCG).** Each layer of the DDN produces multiple target samples, with a selected sample being forwarded as a condition to the next layer. This enables the generation of new samples in the desired direction, ultimately producing a sample that meets the given condition. Indeed, the reconstruction process shown in fig. 1a is a ZSCG process guided by a target image, which never directly enters the network.

To implement ZSCG, we replace the Guided Sampler in fig. 3a with a Conditional Guided Sampler. For instance, when generating an image of class  $y_i$  guided by a classifier  $g_{cls}$ , we replace the “L2 Distance to Training Image” in the Guided Sampler of fig. 3a with the probability of each output image belonging to class  $y_i$  according to the classifier. We then replace “argmin” with “argmax” to construct the Guided Sampler for this classifier. Similar to eq. (1), the sampling method is as follow:

$$k_l^* = \operatorname{argmax}_{k \in \{1, \dots, K\}} g_{cls}(f_l(\mathbf{x}_{l-1}^*[k])[y_i]) \quad (5)$$

After performing  $L$  steps guided sampling and  $L \times K$  steps of classification, the ZSCG results can be obtained without any gradient.

---

#### Algorithm 1 Split-and-Prune of one layer

---

**Require:** Output nodes number  $K$ , model  $f$ , non-output parameters  $\theta$ , target distribution  $q(\mathbf{x})$

- 1: Initialize output node parameters  $\psi(k)$  for  $k \in \{1, \dots, K\}$  with random values
- 2: Initialize counter  $\mathbf{c}(k) = 0$  for  $k \in \{1, \dots, K\}$
- 3: Set split/prune threshold  $P_{split} \leftarrow 2/K$ ,  $P_{prune} \leftarrow 0.5/K$
- 4:  $n \leftarrow 0$ ,  $k_{new} \leftarrow K + 1$
- 5: **repeat**
- 6:    $\mathbf{x} \sim q(\mathbf{x})$
- 7:   Choose  $k^* = \operatorname{argmin}_{k \in \psi} \|f(\theta, \psi(k)) - \mathbf{x}\|^2$
- 8:   Gradient descent  $\nabla_{\theta, \psi(k^*)} \|f(\theta, \psi(k^*)) - \mathbf{x}\|^2$
- 9:    $\mathbf{c}(k^*) := \mathbf{c}(k^*) + 1$
- 10:    $n \leftarrow n + 1$
- 11:    $k_{max} = \operatorname{argmax}_k \mathbf{c}(k)$  and  $k_{min} = \operatorname{argmin}_k \mathbf{c}(k)$
- 12:   **if**  $\mathbf{c}(k_{max})/n > P_{split}$  or  $\mathbf{c}(k_{min})/n < P_{prune}$  **then**
- 13:     # Split:
- 14:      $\psi(k_{new}) := \operatorname{clone}(\psi(k_{max}))$
- 15:      $\mathbf{c}(k_{new}) := \mathbf{c}(k_{max})/2$
- 16:      $\mathbf{c}(k_{max}) := \mathbf{c}(k_{max})/2$
- 17:      $k_{new} \leftarrow k_{new} + 1$
- 18:     # Prune:
- 19:      $n \leftarrow n - \mathbf{c}(k_{min})$
- 20:     remove  $\psi(k_{min})$  and  $\mathbf{c}(k_{min})$
- 21:   **end if**
- 22: **until** converged

---

For super-resolution and colorization tasks, we construct a transform that converts the generated images to the target domain (low-resolution or grayscale). This approach significantly reduces the impact of the missing signal from the condition on the generated images, allowing DDN to successfully perform super-resolution tasks even when the source image has a resolution as low as  $4 \times 4$ .

The use of “argmax” in the Guided Sampler causes each layer to select a fixed sample, resulting in a single image output for each condition, similar to the greedy sampling in GPT. To increase diversity, we employ more flexible sampling methods. For most ZSCG tasks, we use Top-k sampling with  $k = 2$ , balancing diversity and condition appropriateness in the large generation space ( $2^L$ ).

The versatility of ZSCG can be further enhanced by combining different Guided Samplers. For example, an image can guide the primary structure while text guides the attributes. The influence of each condition can be adjusted by setting their respective weights. Experiments involving the combination of different Guided Samplers will be presented in the Appendix.

**Efficient Data Compression Capability.** The latent of DDN is a highly compressed discrete representation, where the information content of a DDN latent is  $L \times \log_2 K$  bits. Taking our default experimental values of  $K=512$  and  $L=128$  as an example, a sample can be compressed to 1152 bits, demonstrating the efficient lossy compression capability of DDN. We hypothesize this ability originates from two aspects: 1) the compact hierarchical discrete representation, and 2) the Split-and-Prune operation makes the probabilities of each node as equal as possible, thereby increasing the information entropy Shannon (1948) of the entire latent distribution and more effectively utilising each bit within the latent.

In our experiments, we set  $K=512$  as the default, considering the balance between generation performance and training efficiency. However, from the perspective of data compression, setting  $K$  to 2 and increasing  $L$  provides a better balance between representation space and compression efficiency. We refer to DDN with  $K=2$  as Binary DDN (BinDDN). To our knowledge, BinDDN are the first generative model capable of directly transforming data into semantically meaningful binary strings. These binary strings represent a leaf node on a balanced binary tree.

### 3.3 TECHNIQUES

In this subsection, we present several techniques for training Discrete Distribution Networks.

**Chain Dropout.** In scenarios where the number of training samples is limited, each data sample undergoes multiple training iterations within the network. During these iterations, similar selections are often made by the Guided Sampler at each layer. However, the representational space of DDN far exceeds the number of training samples in the dataset. This disparity leads to a situation where the network is only trained on a very limited set of pathways, resulting in what can be perceived as overfitting on these pathways. To mitigate this, we introduce a strategy during training where each Discrete Distribution Layer substitutes the Guided Sampler with a “random choice” at a fixed probability rate. We refer to this method as “Chain Dropout”.

**Learning Residual.** In the context of utilizing the Single Shot Generator structure, a Discrete Distribution Layer is introduced every two convolution layers. Given such small amount of computation between adjacent layers, directly regressing the images themselves with these convolutions becomes challenging. Drawing inspiration from ResNet He et al. (2016), we propose a scheme for the network to learn the residual between the output images from the preceding layer and the ground truth. The output of the current layer is then computed as the sum of the output from the previous layer and the current layer’s residual. This approach alleviates the pressure of the network to represent complex data and enhances the flexibility of the network.

**Leak Choice.** In each layer of the DDN, the output is conditioned on the image selected from the previous layer. This condition serves as a signal in the image domain, requiring the current layer to expend computational resources to extract features and interpret the choices made by the Sampler. However, for a DDN with a Single Shot Generator structure, the computation between two adjacent layers is minimal, involving only two convolutional layers. To facilitate faster understanding of the choices made by the Sampler in the subsequent layer, we have added extra convolutional layers to each output node. The features produced by these extra convolutions also serve as conditional inputs to the next layer. But these features don’t participate in the calculation of distance or loss in DDL.

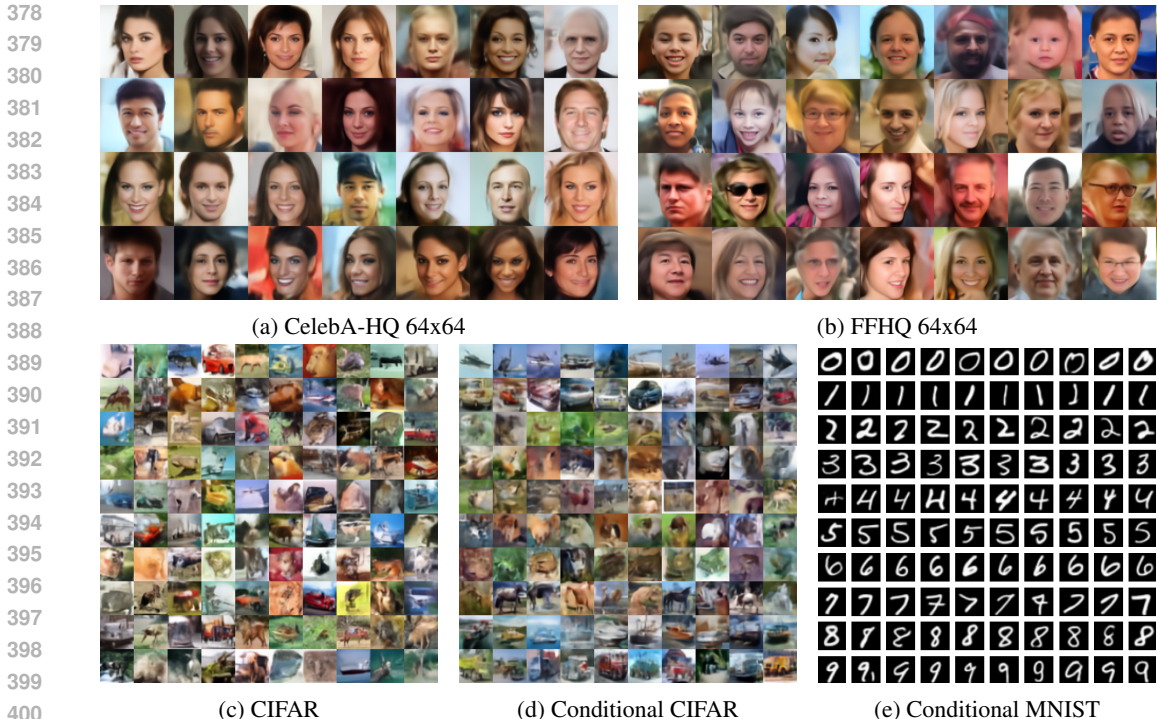


Figure 5: **Random samples from DDN.** Figures (d) and (e) showcase images that are conditionally generated by conditional DDN, with each row of images representing a distinct category.

## 4 EXPERIMENTS

We trained our models on a server equipped with 8 RTX2080Ti GPUs, setting the Chain Dropout probability to 0.05 by default. For the 64x64 resolution experiments, we utilized a DDN with 93M parameters, setting  $K = 512$  and  $L = 128$ . In the CIFAR experiments, we employed a DDN with 74M parameters, setting  $K = 64$  and  $L = 64$ . The MNIST experiments were conducted using a Recurrence Iteration Paradigm UNet model with 407K parameters, where  $K = 64$  and  $L = 10$ . DDN is implemented on the foundation of the EDM Karras et al. (2022) codebase, with training parameters nearly identical to EDM. Both code and model weights shall be released for reproducing. More extended experiments exploring the properties of DDN can be found in the Appendix.

### 4.1 QUALITATIVE AND QUANTITATIVE RESULTS

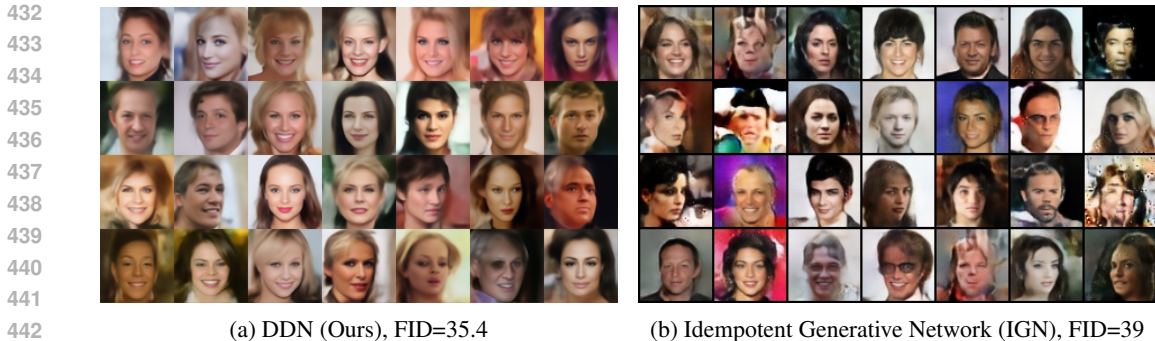
**Generation Quality.** fig. 5a and fig. 5b depict random generation results of DDN on CelebA-HQ-64x64 Karras et al. (2017) and FFHQ-64x64 Karras et al. (2019), verifying the model’s effectiveness in modeling facial data. The generation quality on CelebA-HQ appears superior to that on FFHQ, which is also reflected in the lower FID score (35.4 VS 43.1). We surmise this disparity arises from CelebA-HQ’s relatively cleaner backgrounds and less diverse facial data compared to FFHQ.

We conduct a qualitative comparison with a recent work, the Idempotent Generative Network (IGN) Shocher et al. (2024), accepted by ICLR 2024. Since IGN was only experimented on the CelebA

Table 1: **Quantitative comparison on CIFAR-10.** The data for VQ-VAE comes from Vuong et al. (2023). Data for other baselines comes from Bond-Taylor et al. (2021).

Method	Type	FID↓
DCGAN	GAN	37.1
IGEBM	EBM	38.0
VAE	VAE	106.7
VQ-VAE	VAE	117.4
Gated PixelCNN	AR	65.9
GLOW	Flow	46.0
DDN(ours)	DDN	52.0





444 **Figure 6: Comparison of randomly generated images on CelebA-HQ 64x64.** DDN produces  
445 images with clearer details and fewer artifacts compared to IGN Shocher et al. (2024).  
446

447 dataset and did not release its code, our comparison is limited on the CelebA dataset. As depicted in  
448 fig. 6, our DDN demonstrate better generation capabilities over IGN.  
449

450 Figure 5c showcases the random generation results of DDN on the CIFAR dataset. In parallel,  
451 we present the FID score of DDN on unconditional CIFAR in table 1, comparing it against classical  
452 generative models. It is worth noting that modeling CIFAR remains a challenging task, especially for  
453 new and under-explored generative models like DDN. For instance, the recent work IGN Shocher  
454 et al. (2024) did not conduct experiments on CIFAR. Instead, we wish to emphasize the unique  
455 capability of DDN in “more general zero-shot conditional generation”.

456 **Conditional Training.** Training a conditional DDN is quite straightforward, it only requires the  
457 input of the condition or features of the condition into the network, and the network will automati-  
458 cally learn  $P(X|Y)$ . fig. 5d and fig. 5e show the generation results of the class-conditional DDN on  
459 CIFAR and MNIST, respectively. The conditional DDN displays a good ability to learn the correct  
460  $P(X|Y)$  distribution.

461 **Zero-Shot Conditional Generation.** We  
462 trained a DDN model on the FFHQ-64x64  
463 dataset and then tested the capability of  
464 the model for zero-shot conditional image  
465 generation using the CelebA-HQ-64x64  
466 dataset, as shown in fig. 2. We presented  
467 the experiments of text-guided ZSCG using  
468 CLIP Radford et al. (2021) in the  
469 Appendix. Our generation process does  
470 not require gradient derivation or numeri-  
471 cal optimization, nor does it need iterative  
472 steps. To the best of our knowledge, DDN  
473 is the first generative model that supports  
474 purely discriminative model as guide for  
475 zero-shot conditional generation.

475 In addition, we employed an off-the-shelf  
476 CIFAR classifier Phan (2021) to guide the  
477 generation of specific category images by  
478 a DDN model trained unconditionally on  
479 CIFAR. We want to emphasize that the  
480 classifier is an open-source, pre-trained  
481 ResNet18 model, with no additional mod-  
482 ifications or retraining. fig. 8 displays images of various CIFAR categories generated by the model  
483 under the guidance of the classifier.

484 **Latent analysis.** We trained a DDN on the MNIST dataset with  $K = 8$  and  $L = 3$  to visualize both  
485 the hierarchical generative behavior of the DDN and the distribution of samples in the entire latent  
486 representation space, as shown in Figure 7.

487 **Table 2: Ablation study on FFHQ-64x64.** We use  
488 the reconstruction Fréchet Inception Distance (rFID)  
489 to reflect the reconstructive performance of the network.  
490 All models are trained on the FFHQ-64x64 dataset.  
491 The rFID-FFHQ represents the reconstructive perfor-  
492 mance of the model on the training set, while rFID-  
493 CelebA can be seen as an indication of the model’s gen-  
494 eralization performance on the test set. “w/o” stands  
495 for “without”.

Model	FID↓	FFHQ↓	CelebA↓
K=512 (default)	<b>43.1</b>	<b>26.0</b>	33.2
K=64	47.0	32.3	38.7
K=8	52.6	40.9	49.8
K=2 (BinDDN)	66.5	38.4	70.6
w/o Split-and-Prune	55.3	31.2	34.7
w/o Chain Dropout	182.3	26.5	37.4
w/o Learning Res.	56.2	40.2	40.2
w/o Leak Choice	56.0	34.3	<b>32.2</b>

## 4.2 ABLATION STUDY

In Table 2, we demonstrate the impact of different numbers of output nodes ( $K$ ) and various techniques on the network. Interestingly, despite the substantial difference between having and not having the Split-and-Prune technique in the toy example, as shown in fig. 17, the performance in the ablation study without Split-and-Prune is not as poor as one might expect. We hypothesize that this is due to the Chain Dropout forcing all dead nodes to receive gradient guidance, preventing the network from generating poor results that are unoptimized. A particular case is when  $K = 2$ , where the representational space of BinDDN is already sufficiently compact. The use of Chain Dropout in this case tends to result in more blurred generated images. Therefore, we did not employ Chain Dropout when  $K = 2$ .

## 5 CONCLUSION

In this paper, we have introduced Discrete Distribution Networks, a generative model that approximates the distribution of training data using a multitude of discrete sample points. DDN exhibits unique property: more general zero-shot conditional generation. We also proposed the Split-and-Prune optimization algorithm and several effective techniques for training DDN. Additionally, we showcase the efficacy of DDN and its intriguing properties through experiments.

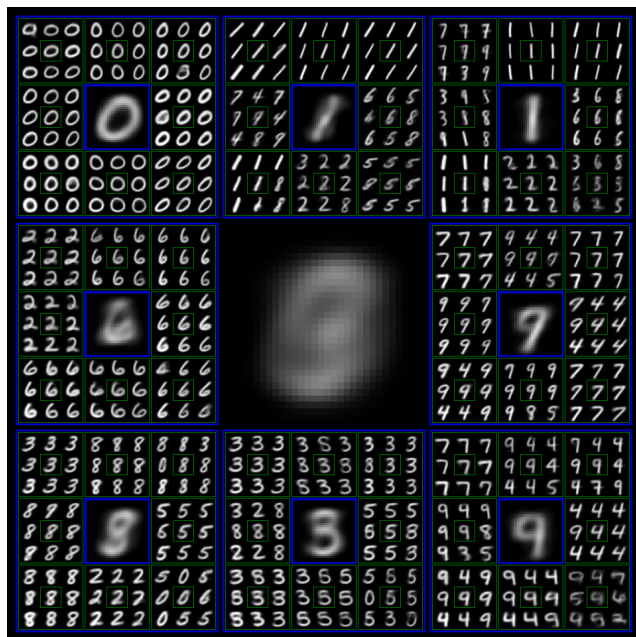


Figure 7: **Hierarchical Generation Visualization of DDN.** We trained a DDN with output level  $L = 3$  and output nodes  $K = 8$  per level on MNIST dataset, its latent hierarchical structure is visualized as recursive grids. Each sample with a colored border represents an intermediate generation product. The samples within the surrounding grid of each colored-bordered sample are refined versions generated conditionally based on it (enclosed by the same color frontier). The small samples without colored borders are the final generated images. The larger the image, the earlier it is in the generation process, implying a coarse version. The large image in the middle is the average of all the generated images. More detailed visualization of  $L = 4$  will be presented in the Appendix.



Figure 8: **Zero-Shot Conditional Generation** on CIFAR-10 Guided by a pretrained classification model without gradient. Each row corresponds to a class in CIFAR-10. Specifically, the first row consists of airplanes, the third row displays birds flying against the blue sky, and the last row presents trucks. Our model successfully generates reasonable images for each class without any conditional training, demonstrating the powerful zero-shot generation capability of our DDN.

## REFERENCES

- 540  
541  
542 Sam Bond-Taylor, Adam Leach, Yang Long, and Chris G Willcocks. Deep generative modelling:  
543 A comparative review of vaes, gans, normalizing flows, energy-based and autoregressive models.  
544 *IEEE transactions on pattern analysis and machine intelligence*, 2021.
- 545 Andrew Brock, Jeff Donahue, and Karen Simonyan. Large Scale GAN Training for High Fidelity  
546 Natural Image Synthesis. *arXiv:1809.11096*, 2019.
- 547 Tom B Brown, Benjamin Mann, Nick Ryder, Melanie Subbiah, Jared Kaplan, Prafulla Dhariwal,  
548 Arvind Neelakantan, Pranav Shyam, Girish Sastry, Amanda Askell, et al. Language models are  
549 few-shot learners. *arXiv preprint arXiv:2005.14165*, 2020.
- 550  
551 Antonia Creswell, Tom White, Vincent Dumoulin, Kai Arulkumaran, Biswa Sengupta, and Anil A  
552 Bharath. Generative adversarial networks: An overview. *IEEE signal processing magazine*, 35  
553 (1):53–65, 2018.
- 554 Prafulla Dhariwal, Heewoo Jun, Christine Payne, Jong Wook Kim, Alec Radford, and Ilya Sutskever.  
555 Jukebox: A generative model for music. *arXiv preprint arXiv:2005.00341*, 2020.
- 556  
557 Patrick Esser, Robin Rombach, and Björn Ommer. Taming Transformers for High-Resolution Image  
558 Synthesis. *arXiv:2012.09841*, 2021. URL <http://arxiv.org/abs/2012.09841>.
- 559 Kartik Goyal, Chris Dyer, and Taylor Berg-Kirkpatrick. Exposing the Implicit Energy Networks  
560 behind Masked Language Models via Metropolis–Hastings. *arXiv:2106.02736*, 2021.
- 561  
562 Alex Graves, Rupesh Kumar Srivastava, Timothy Atkinson, and Faustino Gomez. Bayesian flow  
563 networks. *arXiv preprint arXiv:2308.07037*, 2023.
- 564 Kaiming He, Xiangyu Zhang, Shaoqing Ren, and Jian Sun. Deep Residual Learning for Image  
565 Recognition. In *IEEE CVPR*, 2016.
- 566  
567 Jonathan Ho, Ajay Jain, and Pieter Abbeel. Denoising diffusion probabilistic models, 2020.
- 568 Justin Johnson, Alexandre Alahi, and Li Fei-Fei. Perceptual losses for real-time style transfer and  
569 super-resolution. In *Computer Vision–ECCV 2016: 14th European Conference, Amsterdam, The  
570 Netherlands, October 11–14, 2016, Proceedings, Part II 14*, pp. 694–711. Springer, 2016.
- 571  
572 Tero Karras, Timo Aila, Samuli Laine, and Jaakko Lehtinen. Progressive growing of gans for im-  
573 proved quality, stability, and variation. *arXiv preprint arXiv:1710.10196*, 2017.
- 574 Tero Karras, Samuli Laine, and Timo Aila. A style-based generator architecture for generative  
575 adversarial networks. In *Proceedings of the IEEE/CVF conference on computer vision and pattern  
576 recognition*, pp. 4401–4410, 2019.
- 577  
578 Tero Karras, Miika Aittala, Timo Aila, and Samuli Laine. Elucidating the design space of diffusion-  
579 based generative models. In *Proc. NeurIPS*, 2022.
- 580 Sourabh Katoch, Sumit Singh Chauhan, and Vijay Kumar. A review on genetic algorithm: past,  
581 present, and future. *Multimedia tools and applications*, 80:8091–8126, 2021.
- 582 Diederik P. Kingma and Max Welling. Auto-Encoding Variational Bayes. *ICLR*, 2014.
- 583  
584 Durk P Kingma and Prafulla Dhariwal. Glow: Generative Flow with Invertible 1x1 Convolutions.  
585 *NeurIPS 31*, 2018.
- 586 Alex Krizhevsky, Ilya Sutskever, and Geoffrey E Hinton. Imagenet classification with deep convo-  
587 lutional neural networks. *Advances in neural information processing systems*, 25, 2012.
- 588  
589 Andreas Lugmayr, Martin Danelljan, Andres Romero, Fisher Yu, Radu Timofte, and Luc Van Gool.  
590 Repaint: Inpainting using denoising diffusion probabilistic models. In *Proceedings of the  
591 IEEE/CVF Conference on Computer Vision and Pattern Recognition*, pp. 11461–11471, 2022.
- 592 Chenlin Meng, Yutong He, Yang Song, Jiaming Song, Jiajun Wu, Jun-Yan Zhu, and Stefano Ermon.  
593 Sdedit: Guided image synthesis and editing with stochastic differential equations. *arXiv preprint  
arXiv:2108.01073*, 2021.

- 594 Nithin Gopalakrishnan Nair, Anoop Cherian, Suhas Lohit, Ye Wang, Toshiaki Koike-Akino,  
595 Vishal M Patel, and Tim K Marks. Steered diffusion: A generalized framework for plug-and-  
596 play conditional image synthesis. In *Proceedings of the IEEE/CVF International Conference on*  
597 *Computer Vision*, pp. 20850–20860, 2023.
- 598 Huy Phan. [github.com/huyvnphan/PyTorch\\_CIFAR10](https://github.com/huyvnphan/PyTorch_CIFAR10), January 2021. URL [https://doi.org/](https://doi.org/10.5281/zenodo.4431043)  
599 [10.5281/zenodo.4431043](https://doi.org/10.5281/zenodo.4431043).
- 600 Alec Radford, Luke Metz, and Soumith Chintala. Unsupervised Representation Learning with Deep  
601 Convolutional Generative Adversarial Networks. In *ICLR*, 2016.
- 602 Alec Radford, Jong Wook Kim, Chris Hallacy, Aditya Ramesh, Gabriel Goh, Sandhini Agarwal,  
603 Girish Sastry, Amanda Askell, Pamela Mishkin, Jack Clark, et al. Learning transferable visual  
604 models from natural language supervision. In *International conference on machine learning*, pp.  
605 8748–8763. PMLR, 2021.
- 606 Aditya Ramesh, Prafulla Dhariwal, Alex Nichol, Casey Chu, and Mark Chen. Hierarchical text-  
607 conditional image generation with clip latents. *ArXiv*, abs/2204.06125, 2022. URL [https://](https://api.semanticscholar.org/CorpusID:248097655)  
608 [api.semanticscholar.org/CorpusID:248097655](https://api.semanticscholar.org/CorpusID:248097655).
- 609 Ali Razavi, Aaron Van den Oord, and Oriol Vinyals. Generating diverse high-fidelity images with  
610 vq-vae-2. *Advances in neural information processing systems*, 32, 2019.
- 611 Robin Rombach, A. Blattmann, Dominik Lorenz, Patrick Esser, and Björn Ommer. High-  
612 resolution image synthesis with latent diffusion models. *2022 IEEE/CVF Conference on Com-*  
613 *puter Vision and Pattern Recognition (CVPR)*, pp. 10674–10685, 2021. URL [https://api.](https://api.semanticscholar.org/CorpusID:245335280)  
614 [semanticscholar.org/CorpusID:245335280](https://api.semanticscholar.org/CorpusID:245335280).
- 615 Chitwan Saharia, William Chan, Huiwen Chang, Chris A. Lee, Jonathan Ho, Tim Salimans,  
616 David J. Fleet, and Mohammad Norouzi. Palette: Image-to-image diffusion models. *ACM SIG-*  
617 *GRAPH 2022 Conference Proceedings*, 2021. URL [https://api.semanticscholar.](https://api.semanticscholar.org/CorpusID:243938678)  
618 [org/CorpusID:243938678](https://api.semanticscholar.org/CorpusID:243938678).
- 619 Claude Elwood Shannon. A mathematical theory of communication. *The Bell system technical*  
620 *journal*, 27(3):379–423, 1948.
- 621 Assaf Shocher, Amil Dravid, Yossi Gandelsman, Inbar Mosseri, Michael Rubinstein, and Alexei A  
622 Efros. Idempotent generative network. In *ICLR*, 2024.
- 623 Jiaming Song, Chenlin Meng, and Stefano Ermon. Denoising Diffusion Implicit Models. In *ICLR*,  
624 2021.
- 625 Aaron van den Oord, Nal Kalchbrenner, Lasse Espeholt, koray kavukcuoglu, Oriol Vinyals, and  
626 Alex Graves. Conditional Image Generation with PixelCNN Decoders. *NeurIPS* 29, 2016.
- 627 Aäron Van Den Oord, Nal Kalchbrenner, and Koray Kavukcuoglu. Pixel Recurrent Neural Net-  
628 works. In *ICML*, 2016. ISBN 978-1-5108-2900-8.
- 629 Aaron van den Oord, Oriol Vinyals, and Koray Kavukcuoglu. Neural discrete representation learn-  
630 ing, 2018.
- 631 Andrey Voynov, Kfir Aberman, and Daniel Cohen-Or. Sketch-guided text-to-image diffusion  
632 models. *ACM SIGGRAPH 2023 Conference Proceedings*, 2022. URL [https://api.](https://api.semanticscholar.org/CorpusID:254018130)  
633 [semanticscholar.org/CorpusID:254018130](https://api.semanticscholar.org/CorpusID:254018130).
- 634 Long Tung Vuong, Trung Le, He Zhao, Chuanxia Zheng, Mehrtash Harandi, Jianfei Cai, and  
635 Dinh Phung. Vector quantized Wasserstein auto-encoder. In Andreas Krause, Emma Brun-  
636 skill, Kyunghyun Cho, Barbara Engelhardt, Sivan Sabato, and Jonathan Scarlett (eds.), *Pro-*  
637 *ceedings of the 40th International Conference on Machine Learning*, volume 202 of *Proce-*  
638 *edings of Machine Learning Research*, pp. 35223–35242. PMLR, 23–29 Jul 2023. URL [https://](https://proceedings.mlr.press/v202/vuong23a.html)  
639 [proceedings.mlr.press/v202/vuong23a.html](https://proceedings.mlr.press/v202/vuong23a.html).
- 640 Yinhuai Wang, Jiwen Yu, and Jian Zhang. Zero-shot image restoration using denoising diffusion  
641 null-space model. *arXiv preprint arXiv:2212.00490*, 2022.

648 Will Williams, Sam Ringer, Tom Ash, David MacLeod, Jamie Dougherty, and John Hughes. Hier-  
649 archical quantized autoencoders. *Advances in Neural Information Processing Systems*, 33:4524–  
650 4535, 2020.

651  
652 Jiwen Yu, Yinhuai Wang, Chen Zhao, Bernard Ghanem, and Jian Zhang. Freedom: Training-free  
653 energy-guided conditional diffusion model. In *Proceedings of the IEEE/CVF International Con-  
654 ference on Computer Vision*, pp. 23174–23184, 2023.

655  
656 Lvmin Zhang, Anyi Rao, and Maneesh Agrawala. Adding conditional control to text-to-image  
657 diffusion models. *ArXiv*, abs/2302.05543, 2023. URL [https://api.semanticscholar.  
658 org/CorpusID:256827727](https://api.semanticscholar.org/CorpusID:256827727).

659 Richard Zhang, Phillip Isola, Alexei A. Efros, Eli Shechtman, and Oliver Wang. The Unreasonable  
660 Effectiveness of Deep Features as a Perceptual Metric. In *IEEE CVPR*, 2018.

## 663 A EXPERIMENTAL RESULTS ON GENERATIVE PERFORMANCE

664  
665 We present additional experiments to verify the generative and reconstructive capabilities of Discrete  
666 Distribution Networks (DDN).

667  
668 **Conditional DDN for Image-to-Image Tasks.** In the realm of image-to-image tasks, we extend our  
669 Discrete Distribution Networks (DDN) to a conditional setting, resulting in the conditional DDN.  
670 In this architecture, the condition is directly fed into the network during training in the beginning  
671 of each stage. The condition serves as an informative guide, significantly reducing the model’s  
672 generative space and, consequently, the complexity of the modeling task.

673 Those conditions inherently carry rich information, enabling the network to produce higher-quality  
674 samples. Through this conditional design, the DDN can leverage the abundant information contained  
675 in the conditions to generate more accurate and detailed images as shown in fig. 9.

676 **Verify whether DDN can generate new images.** As depicted in fig. 10, we compare the images  
677 that are closest in the training dataset, FFHQ, to those generated by our DDNs. It suggests that our  
678 DDNs can synthesize new images that, while not present in the original dataset, still conform to its  
679 target distribution.

680 **Demonstration of Generation and Reconstruction Quality.** figs. 12 to 14 illustrate the generation  
681 and reconstruction results in various ablation experiments using the DDN model.

682  
683 **Efficacy of Split-and-Prune and Chain Dropout.** A series of experiments were conducted to sep-  
684 arately investigate the effectiveness of the Split-and-Prune and Chain Dropout methods. To isolate  
685 the impacts of these two algorithms, we simplified the experimental conditions as much as possible,  
686 using the MNIST dataset as a base, setting  $K = 8$  and  $L = 10$ , and disabling Learning Residual.  
687 The generated image quality under three different settings is displayed in fig. 11. The results demon-  
688 strated that the Split-and-Prune method is indispensable, leading to significant improvements in the  
689 quality of generated images. Meanwhile, the Chain Dropout method was found to alleviate the poor  
690 results observed when the Split-and-Prune method was not implemented.

## 691 B FURTHER DEMONSTRATIONS ON ZERO-SHOT CONDITIONAL 692 GENERATION

693  
694  
695 In this section, we present additional experimental results on Zero-Shot Conditional Generation  
696 (ZSCG).

697 **Utilizing CLIP as Conditioning Guidance.** As illustrated in fig. 15, we leverage CLIP Radford  
698 et al. (2021) along with corresponding prompts as conditioning cues. We use a Discrete Distribution  
699 Network (DDN) model, which is exclusively trained on the FFHQ dataset, to yield Zero-Shot Con-  
700 ditional Generation (ZSCG) results. Remarkably, DDN can generate corresponding images under  
701 the guidance of CLIP without the necessity for gradient computations and only requiring a single  
inference pass.

702  
703  
704  
705  
706  
707  
708  
709  
710  
711  
712  
713  
714  
715  
716  
717  
718  
719  
720  
721  
722  
723  
724  
725  
726  
727  
728  
729  
730  
731  
732  
733  
734  
735  
736  
737  
738  
739  
740  
741  
742  
743  
744  
745  
746  
747  
748  
749  
750  
751  
752  
753  
754  
755

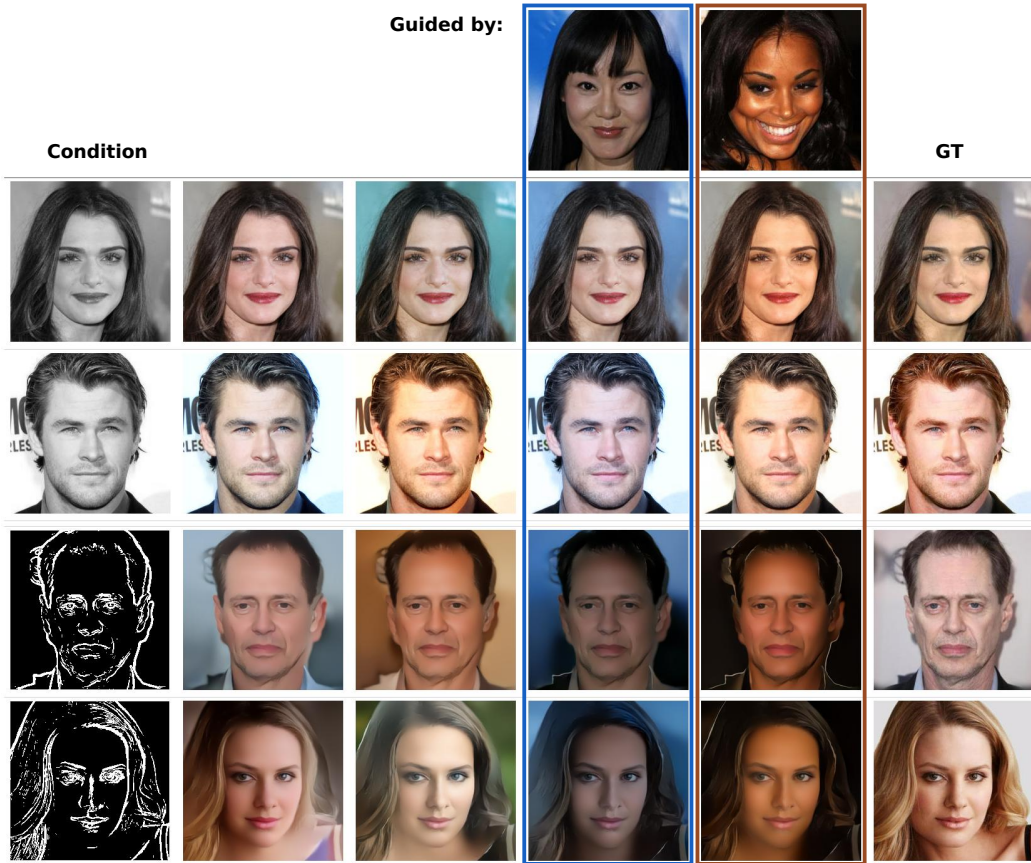


Figure 9: **Conditional DDN performing coloring and edge-to-RGB tasks.** Benefiting from the reduction of the generative space by the condition, DDN is capable of generating high-quality images of  $256 \times 256$  resolution. Columns 4 and 5 display the generated results under the guidance of other images, where the produced image strives to adhere to the style of the guided image as closely as possible while ensuring compliance with the condition.

756  
757  
758  
759  
760  
761  
762  
763  
764  
765  
766  
767  
768  
769  
770  
771  
772  
773  
774  
775  
776  
777  
778  
779  
780  
781  
782  
783  
784  
785  
786  
787  
788  
789  
790  
791  
792  
793  
794  
795  
796  
797  
798  
799  
800  
801  
802  
803  
804  
805  
806  
807  
808  
809



Figure 10: Nearest neighbors of the model trained on FFHQ. The leftmost column presents images generated by the DDN. Starting from the second column, we display the images from FFHQ that are most similar to the generated images, as measured by LPIPS Zhang et al. (2018).

810  
811  
812  
813  
814  
815  
816  
817  
818  
819  
820  
821  
822  
823  
824  
825  
826  
827  
828  
829  
830  
831  
832  
833  
834  
835  
836  
837  
838  
839  
840  
841  
842  
843  
844  
845  
846  
847  
848  
849  
850  
851  
852  
853  
854  
855  
856  
857  
858  
859  
860  
861  
862  
863

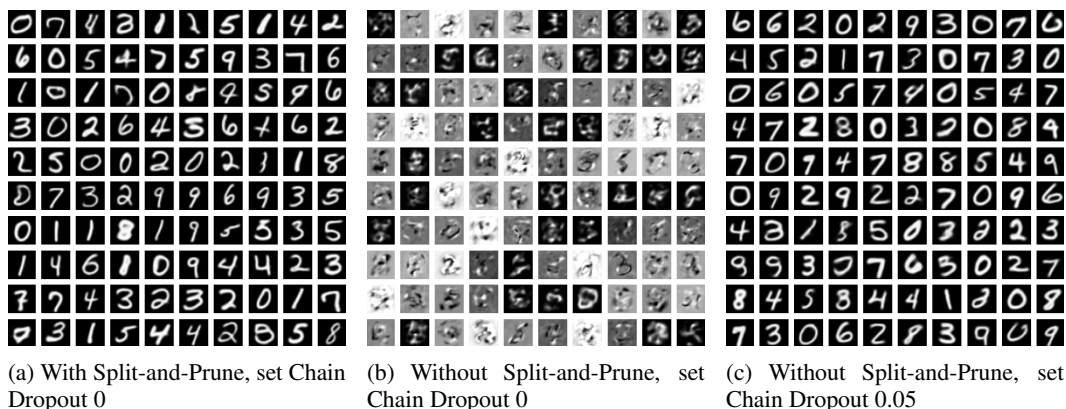


Figure 11: Efficacy of Split-and-Prune and Chain Dropout on MNIST.



Figure 12: Illustration of the random sample generation effects as part of the ablation study on our DDNs model.



864  
865  
866  
867  
868  
869  
870  
871  
872  
873  
874  
875  
876  
877  
878  
879  
880  
881  
882  
883  
884  
885  
886  
887  
888  
889  
890  
891  
892  
893  
894  
895  
896  
897  
898  
899  
900  
901  
902  
903  
904  
905  
906  
907  
908  
909  
910  
911  
912  
913  
914  
915  
916  
917

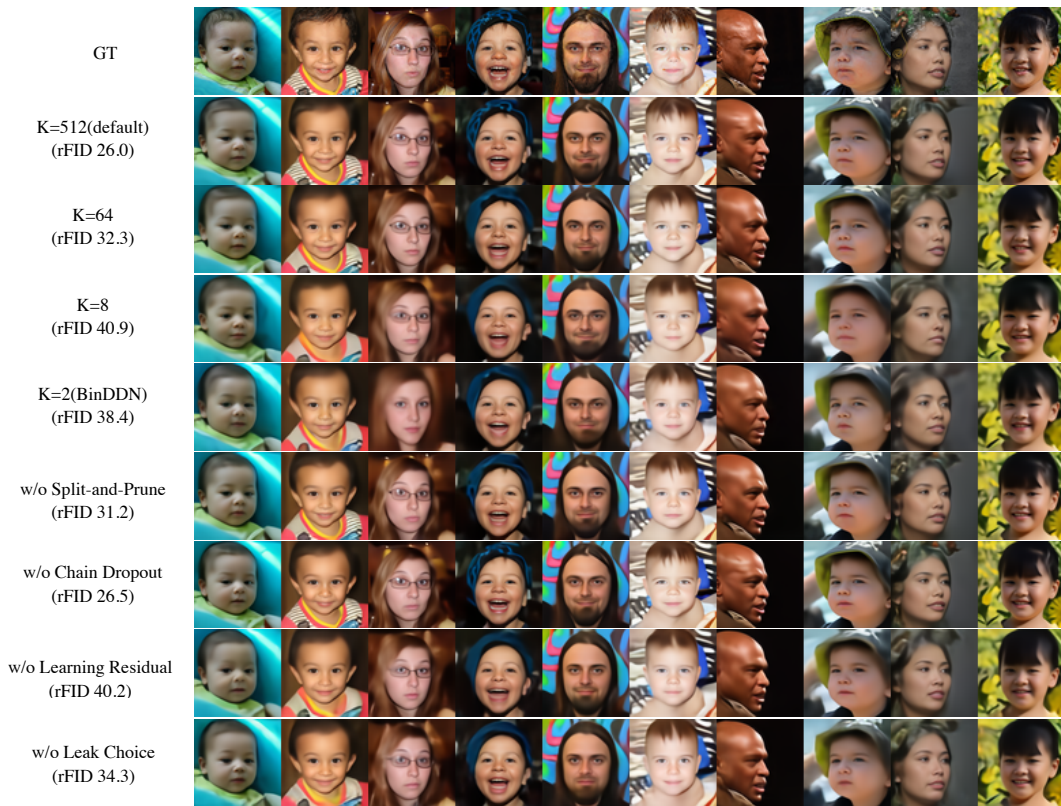
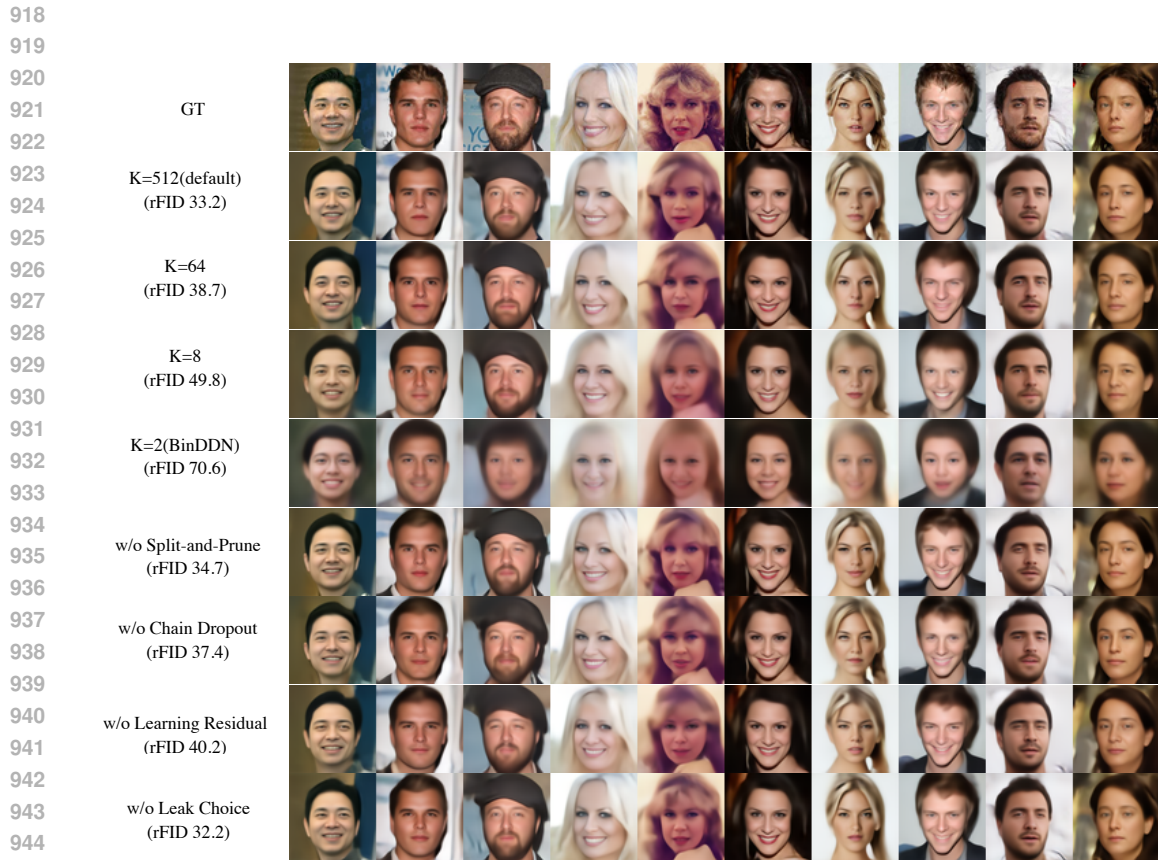


Figure 13: Demonstration of the reconstruction capability of our ablation study model on FFHQ-64x64, which can be interpreted as the model’s fitting ability on the training set.



946  
947  
948  
949  
950  
951  
952  
953  
954  
955  
956  
957  
958  
959  
960  
961  
962  
963  
964  
965  
966  
967  
968  
969  
970  
971

Figure 14: Demonstration of the reconstruction capability of our ablation study model on CelebA-64x64, which can be interpreted as the model’s generalization ability on the test set.

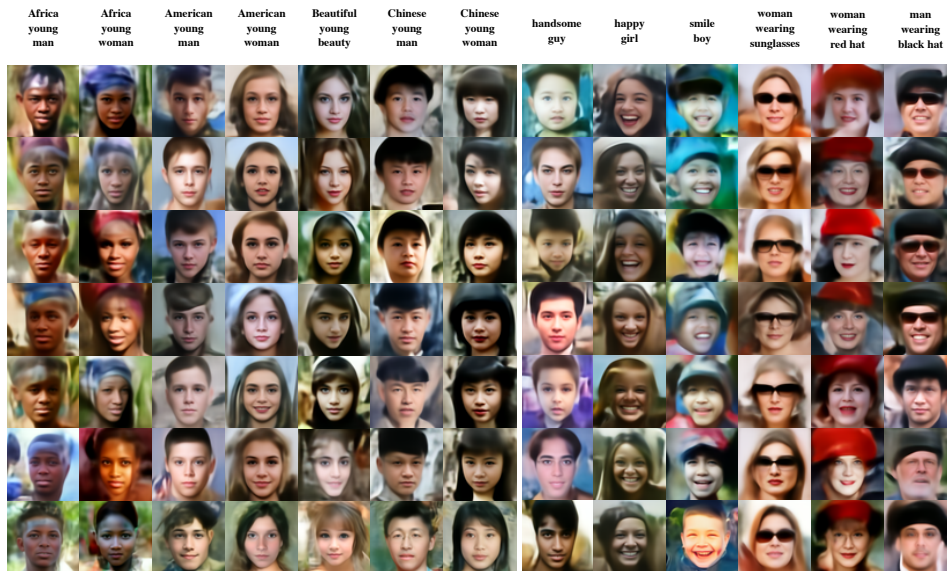


Figure 15: **Zero-Shot Conditional Generation** guided by CLIP. The text at the top is the guide text for that column.



Figure 16: **Zero-Shot Conditional Generation under the Influence of Multiple Conditions.** The DDN balances the steering forces of CLIP and Inpainting according to their associated weights.

Nodes/level	Level	Representation space	Validation accuracy↑			
			128	1024	10k	50k
K	L	$K^L$	65.9	77.3	85.8	86.9
2	10	1024	65.9	77.3	85.8	86.9
8	3	512	<b>69.0</b>	<b>81.1</b>	<b>87.6</b>	88.0
8	5	$3.3 \times 10^4$	67.5	79.1	87.5	<b>90.5</b>
8	10	$1.1 \times 10^9$	58.6	75.3	84.9	89.0
64	10	$1.1 \times 10^{18}$	52.5	70.4	80.9	86.3

Table 3: **Fine-tuning DDN latent as decision tree on MNIST.** Constructing a decision tree based on the latent variables from the DDN and fine-tuning it on MNIST training set. We report the validation set accuracy of the decision tree after majority voting for class prediction with varying number of training samples: 128, 1,024, 10,000, and 50,000 (the full training set).

**ZSCG with Multiple Conditions.** In fig. 16, we illustrate the operation of ZSCG under the combined action of two Guided Samplers: Inpainting and CLIP. Each sampler operates under its own specific condition. The inpainting sampler utilizes a mask to cover the areas where the CLIP prompt acts. Specifically, “wearing sunglasses” masks the eyes, “wearing a hat” masks the upper half of the face, and “happy person” masks the lower half. For each Discrete Distribution Layer (DDL), both samplers assign a rank to the generated images, corresponding to the degree of match to their respective conditions– the better the match, the higher the rank. We assign a weight to each sampler, which affects the assigned ranking. In this case, both samplers have a weight of 0.5. To promote diversity in the generated samples, we randomly select one image from the top two ranked by their condition-matching scores, serving as the output for that DDL layer.

## C LATENT ANALYSIS

**Semantic Performance of Latents.** We explored the semantic capabilities of DDN latents through a classification experiment on the MNIST dataset. Given the inherent tree structure of DDN’s latents, we employed a decision tree classification method, using fine-tuning data to assign class votes to nodes in the tree. For unassigned nodes, their class is inherited from the closest ancestor node with a class. We fine-tuned DDN’s latent decision tree using various numbers of labeled training set data, and the results on the test set are shown in table 3. All experiments in this table were conducted with Recurrence Iteration Paradigm’s UNet, which has approximately 407k parameters. However, computational complexity increases proportionally with the number of output levels (L). These experiments substantiate that DDN’s latents encompass meaningful semantic information.

**More Comprehensive Latent Visualization.** fig. 18 demonstrates a more comprehensive distribution of samples that correspond to the latent variables.

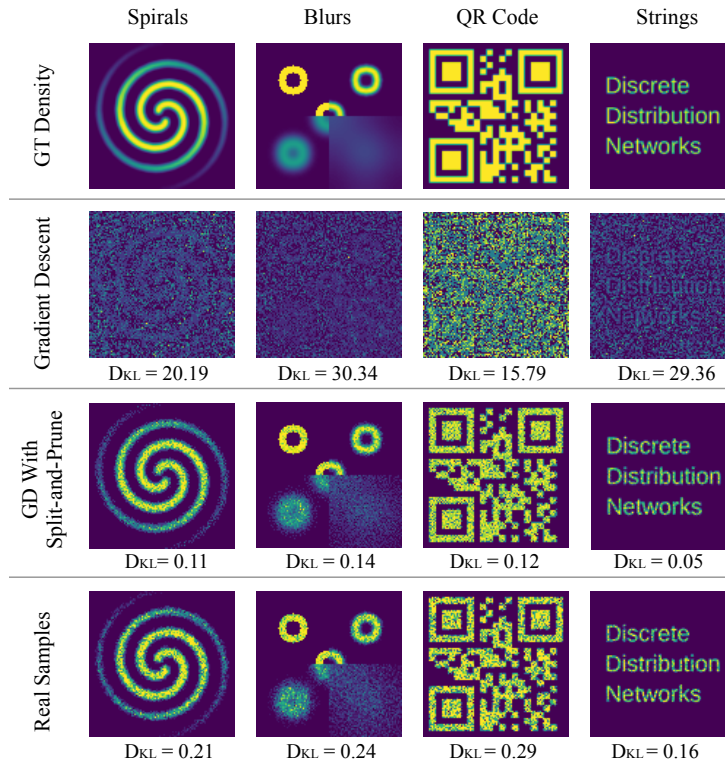


Figure 17: **Toy examples for two-dimensional data generation.** The numerical values at the bottom of each figure represent the Kullback-Leibler (KL) divergence. Due to phenomena such as “dead nodes” and “density shift”, the application of Gradient Descent alone fails to properly fit the Ground Truth (GT) density. By employing the Split-and-Prune strategy, the density map looks the same as Real Samples. In the experiment, we use  $K = 10,000$  discrete nodes to emulate the probability distribution of GT density. Each node encompasses two parameters,  $x$  and  $y$ , initialized from a uniform distribution. Each experiment consists of 100,000 iterations, where in each iteration an L2 loss is calculated based only on the node closest to the GT. The GT density map is converted into a discrete distribution with bins of size  $100 \times 100$ , which is then used to calculate the KL divergence against the discrete distribution represented by these nodes. The KL divergence of Split-and-Prune is even lower than that of the Real Samples. This is because our algorithm has been exposed to 100,000 sets of GT data, thus it better reflects the GT distribution compared to the ‘Real Samples’, which are drawn only 10,000 times from the GT distribution.

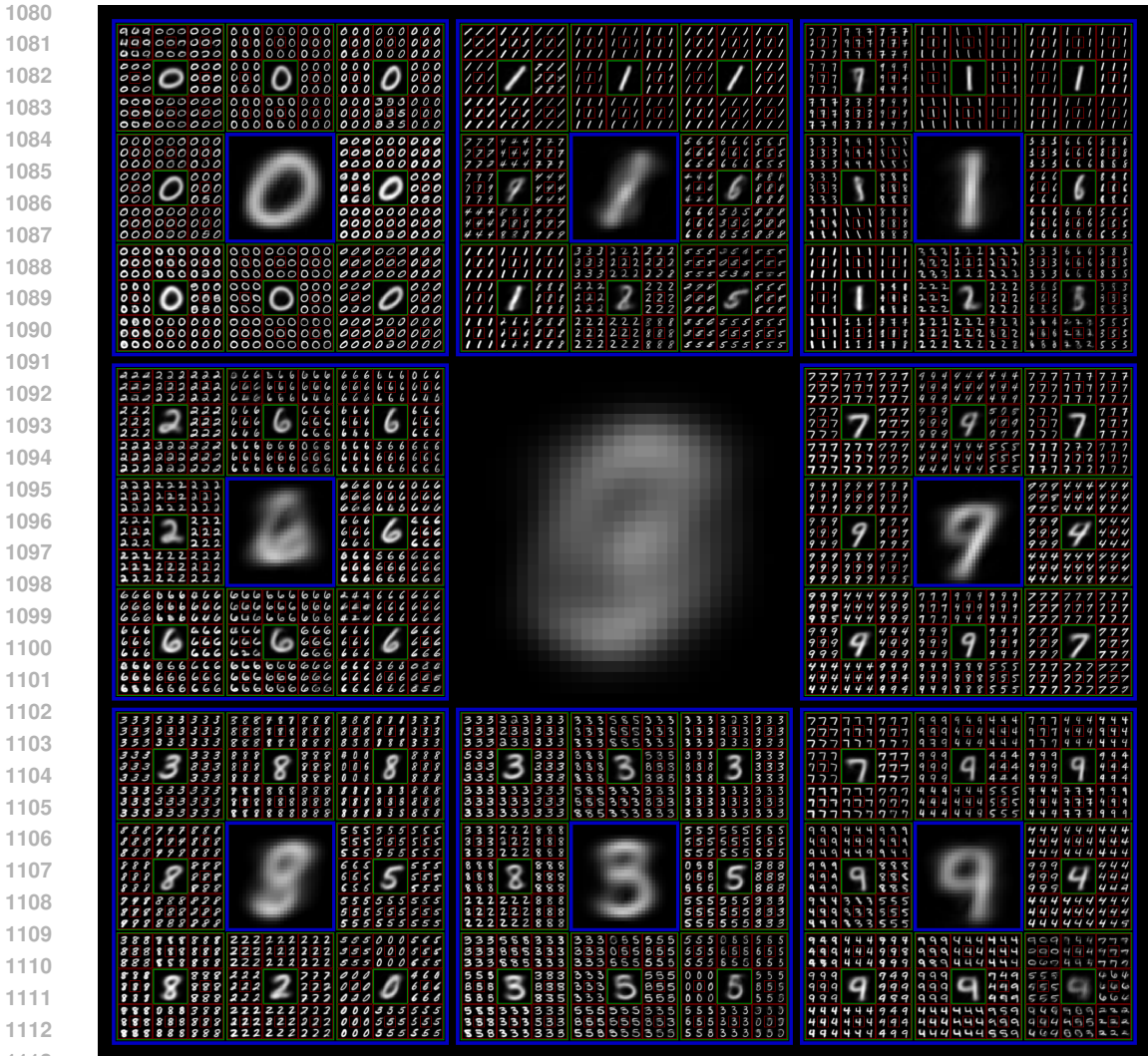


Figure 18: **Hierarchical Generation Visualization of DDN with  $L = 4$ .** We trained a DDN with output level  $L = 4$  and output nodes  $K = 8$  per level on MNIST dataset, its latent hierarchical structure is visualized as recursive grids. Each sample with a colored border represents an intermediate generation product. The samples within the surrounding grid of each colored-bordered sample are refined versions generated conditionally based on it (enclosed by the same color frontier). The small samples without colored borders are the final generated images. The larger the image, the earlier it is in the generation process, implying a coarse version. The large image in the middle is the average of all the generated images. The samples with blue borders represent the 8 outputs of the first level, while those with green borders represent the  $8^2 = 64$  outputs of the second level. It can be observed that images within the same grid display higher similarity, due to their shared “ancestors”. Best view in color and zoom in.

### D MORE DETAILED EXPERIMENTAL EXPLANATION

In fig. 19, we have expanded the “Illustration of the Split-and-Prune operation” by providing a schematic when  $K$  increases to 15. This demonstrates that having a larger sample space results in an approximation that is closer to the target distribution.

In the caption of fig. 17, we have detailed the experimental parameters for “Toy examples for two-dimensional data generation”. Additionally, we will explain why the KL divergence in our model is lower than that found in the Real Samples.

1134  
1135  
1136  
1137  
1138  
1139  
1140  
1141  
1142  
1143  
1144  
1145  
1146  
1147  
1148  
1149  
1150  
1151  
1152  
1153  
1154  
1155  
1156  
1157  
1158  
1159  
1160  
1161  
1162  
1163  
1164  
1165  
1166  
1167  
1168  
1169  
1170  
1171  
1172  
1173  
1174  
1175  
1176  
1177  
1178  
1179  
1180  
1181  
1182  
1183  
1184  
1185  
1186  
1187

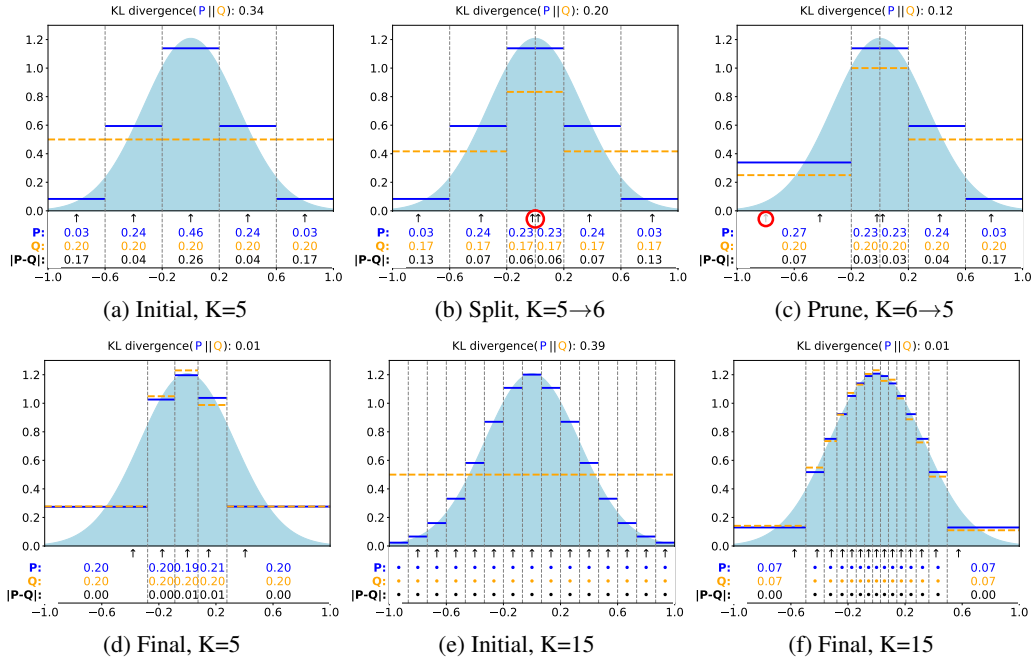


Figure 19: **Illustration of the Split-and-Prune operation.** For example in (a), the light blue bell-shaped curve represents a one-dimensional target distribution. The 5 “↑” under the x-axis are the initial values from a uniform distribution of 5 output nodes, which divide the entire space into 5 parts using midpoints between adjacent nodes as boundaries (i.e., vertical gray dashed lines). Each part corresponds to the range represented by this output node on the continuous space  $x$ . Below each node are three values:  $P$  stands for the relative frequency of the ground truth falling within this node’s range during training;  $Q$  refers to the probability mass of this sample (node) in the discrete distribution output by the model during the generation phase, which is generally equal for each sample, i.e.,  $1/K$ . The bottom-most value denotes the difference between  $P$  and  $Q$ . Colorful horizontal line segments represent the average probability density of  $P$ ,  $Q$  within corresponding intervals. In (b), the Split operation selects the node with the highest  $P$  (circled in red). In (c), the Prune operation selects the node with the smallest  $P$  (circled in red). In (d), through the combined effects of loss and Split-and-Prune operations, the distribution of output nodes moves towards final optimization. From the observed results, the KL divergence  $(KL(P||Q))$  consistently decreases as the operation progresses, and the yellow line increasingly approximates the light blue target distribution. Finally, we show the distributions of the initial and final stages when the number of output nodes  $K = 15$  in (e) and (f). Due to the increased representational space (higher resolution), in (f), the probability density distribution  $Q$  (yellow line segment) is closer to the lightblue target distribution than in the case of  $K = 5$ .

1188 E LIMITATIONS  
11891190 There are some key limitations of Discrete Distribution Networks (DDNs):  
1191

- 1192 • **Loss of high-frequency signals:** The high level of data compression and the use of pixel  
1193 L2 loss during optimization may result in the loss of high-frequency signals, causing the  
1194 images to appear blurred. A potential improvement could be learning from VQ-GAN Esser  
1195 et al. (2021) and incorporating adversarial loss Creswell et al. (2018) to enhance the mod-  
1196 eling of high-frequency signals.
- 1197 • **Difficulty with complex data:** While random choice can generate decent facial data,  
1198 DDNs struggle with complex data, such as ImageNet Krizhevsky et al. (2012). One possi-  
1199 ble solution is to learn an additional prior model dedicated to sampling output nodes.
- 1200 • **computational burden of zero-shot conditional generation:** ZSCG requires  $L \times K$  for-  
1201 ward passes through the guided model, where  $L$  is the number of layers and  $K$  is the  
1202 number of possible outputs per layer. When the guided model itself is computationally ex-  
1203 pensive, this results in significant computational overhead and prolonged generation time.  
1204 However, since the discrimination process is parallelizable across the  $K$ -dimensional out-  
1205 put space, batching techniques can be employed to mitigate latency. In addition, further  
1206 research will be conducted to reduce the number of guided model calls during the ZSCG  
1207 process.

1208  
1209  
1210  
1211  
1212  
1213  
1214  
1215  
1216  
1217  
1218  
1219  
1220  
1221  
1222  
1223  
1224  
1225  
1226  
1227  
1228  
1229  
1230  
1231  
1232  
1233  
1234  
1235  
1236  
1237  
1238  
1239  
1240  
1241